

Multiscale modeling of ultrafast melting phenomena

Gaetano Calogero, Domenica Raciti, Pablo Acosta, Fuccio Cristiano, Ioannis Deretzis, Giuseppe Fisicaro, Karim Huet, Sebastien Kerdiles, Alberto Sciuto, Antonino La Magna

▶ **To cite this version:**

Gaetano Calogero, Domenica Raciti, Pablo Acosta, Fuccio Cristiano, Ioannis Deretzis, et al.. Multiscale modeling of ultrafast melting phenomena. npj Computational Materials, 2022, 8, pp.1-10. 10.1038/s41524-022-00720-y . hal-03795924

HAL Id: hal-03795924
https://laas.hal.science/hal-03795924

Submitted on 4 Oct 2022

HAL is a multi-disciplinary open access archive for the deposit and dissemination of scientific research documents, whether they are published or not. The documents may come from teaching and research institutions in France or abroad, or from public or private research centers.

L'archive ouverte pluridisciplinaire **HAL**, est destinée au dépôt et à la diffusion de documents scientifiques de niveau recherche, publiés ou non, émanant des établissements d'enseignement et de recherche français ou étrangers, des laboratoires publics ou privés.

npj Computational Materials

www.nature.com/npjcompumats

ARTICLE OPEN

Check for updates

Multiscale modeling of ultrafast melting phenomena

Gaetano Calogero[1]✉, Domenica Raciti[1], Pablo Acosta-Alba[2], Fuccio Cristiano[3], Ioannis Deretzis[1], Giuseppe Fisicaro[1], Karim Huet[4], Sébastien Kerdilès[2], Alberto Sciuto[1,5] and Antonino La Magna[1]✉

Ultraviolet Nanosecond Laser Annealing (LA) is a powerful tool for both fundamental investigations of ultrafast, nonequilibrium phase-change phenomena and technological applications (e.g., the processing of 3D sequentially integrated nano-electronic devices) where strongly confined heating and melting is desirable. Optimizing the LA process along with the experimental design is challenging, especially when involving complex 3D-nanostructured systems with various shapes and phases. To this purpose, it is essential to model critical nanoscale physical LA-induced phenomena, such as shape changes or formation and evolution of point and extended defects. To date, LA simulators are based on continuum models, which cannot fully capture the microscopic kinetics of a solid–liquid interface. In this work a fully atomistic LA simulation methodology is presented, based on the parallel coupling of a continuum, finite elements, μm-scale electromagnetic-thermal solver with a super-lattice Kinetic Monte Carlo atomistic model for melting. Benchmarks against phase-field models and experimental data validate the approach. LA of a Si(001) surface is studied varying laser fluence and pulse shape, assuming both homogeneous and inhomogeneous nucleation, revealing how liquid Si nuclei generate, deform and coalesce during irradiation. The proposed methodology is applicable to any system where the atom kinetics is determined by a strongly space- and time-dependent field, such as temperature or strain.

npj Computational Materials (2022)8:36 ; https://doi.org/10.1038/s41524-022-00720-y

INTRODUCTION

The ability of heating and melting solid materials over small space- and time scales allows for accessing the early stages of the melting phenomenon, characterized by the nucleation of the molten phase and the ultra-rapid liquid nuclei kinetics[1,2]. In the case of crystalline solids the random character of the nuclei formation is accompanied by an orientation-dependent evolution mechanism that binds the shape of nano-droplets to the symmetry of the hosting solid substrate. These features are self-evident in, e.g., Fig. 1 where experimental snapshots of close-to-nucleation states are obtained by means of melting irradiation processes at critical energy density values[3].

In addition to the fundamental understanding in the phase transitions and nonequilibrium phenomena fields, controlling the microstructural evolution in the case of Si, SiGe, and other group IV semiconductors is becoming essential for the low-temperature processing of next generation micro- and nano-electronic devices. For instance, 3D sequential integration processes rely on the possibility of annealing the regions of the device near the surface while keeping the temperature of embedded fabricated layers as low as possible[4–9]. To this regard, using pulsed laser beams with wavelength in the ultraviolet range and nanosecond pulse duration is attracting much interest, as it allows for structural modifications, alloy fraction manipulation, and also dopants redistribution and activation without degrading the performance of the underlying active layers in the 3D stacks[6,9–14]. The main technological challenge is to design the nanosecond laser annealing (LA) process together with the device design, in order to optimize the topography and the materials' choice, not only in 3D sequentially integrated architectures, but also in other complex patterned structures, featuring low-dimensional, nm-sized elements with various shapes and phases[12–14]. Tackling this challenge requires predictive simulation tools, with reliable calibrations for the materials of interest, able to model the relevant physical phenomena at various length and time scales while keeping the computational cost affordable. Current simulation codes are based on continuum models, which allow for an efficient solution of coupled partial differential equations (PDEs) governing the laser-matter interaction, and are nowadays massively used in industrial and academic environments[9,13–19]. However, these are unable to faithfully model important physical phenomena occurring at the nanoscale in the material under laser irradiation, such as shape deformations[11,20], defect generation and evolution[21–24], stress relaxation[9,11,25], or explosive recrystallization[10,14,26–28], for which a resolution at the atomic level is necessary. Investigating the origin of such effects, corroborating their experimental observation and reliably predicting routes to control them is therefore a blind spot of state-of-the-art tools, and calls for development of unconventional LA simulation methodologies able to effectively model the atom-by-atom kinetics governing melting and regrowth induced by the laser pulse.

In this work we present a tool for fully atomistic simulations of phase transitions occurring during an LA process of group IV elemental or compound semiconductors, such as Si, Ge, SiGe, and more. It is based on a multiscale algorithm that seamlessly couples a continuum model, based on the finite element method (FEM), for self-consistently solving the electromagnetic (Maxwell) and heat diffusion (Fourier) problem of an irradiated 3D-nanostructured system with an atomistic super-lattice kinetic Monte Carlo (KMC) model. Such multiscale methodology allows to simulate with atomic resolution the evolution of liquid-solid interfaces during LA, enabling one to account for all types of features which cannot be captured using a fully continuum description. The formalism presented here is applicable to any system where the atoms kinetics depends strongly on an external space- and/or time-dependent field, such as temperature or strain. First, we present the theoretical details of the methodology. Then, a benchmark against continuum phase-field models and

[1]CNR IMM, Catania, Italy. [2]Université Grenoble Alpes, CEA-LETI, Grenoble, France. [3]LAAS, CNRS, Université de Toulouse, Toulouse, France. [4]Laser Systems & Solutions of Europe (LASSE), Gennevilliers, France. [5]Dipartimento di Fisica e Astronomia, Università di Catania, Catania, Italy. ✉email: gaetano.calogero@imm.cnr.it; antonino.lamagna@imm.cnr.it

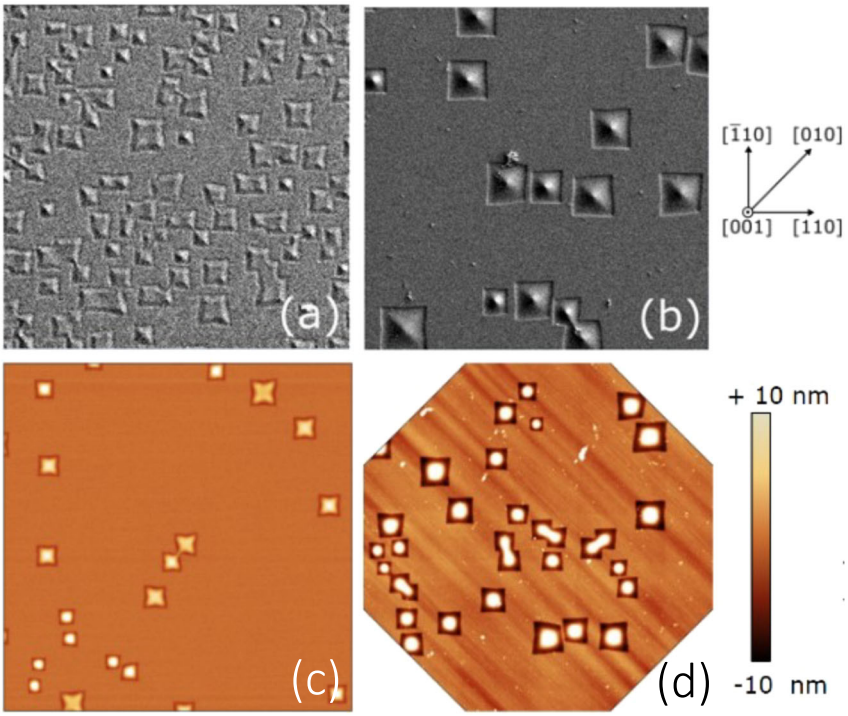


Fig. 1 Experimental measurements of close-to-nucleation states generated by laser annealing at a critical energy density. a Scanning electron microscopy $5 \times 5\ \mu m^2$ images of bulk Si(001) after LA at $1.88\ J\ cm^{-2}$ laser fluence and (**b**) 1300-nm-thick Ge epilayer on Si after LA at $0.83\ J\ cm^{-2}$, both within the surface melt regime. Atomic force microscopy $5 \times 5\ \mu m^2$ images (different areas) of the same Si and Ge samples are reported in (**c**, **d**), respectively. The laser wavelength is 308 nm and the pulse duration is ~146 ns. For these precise conditions the maximum temperature exceeds the materials' melting points at the surface proximity and for a few nanoseconds lasting transient. As a consequence visual snapshots of the solid/liquid nucleation stage are obtained. We note that square-shaped hillocks with ⟨110⟩-aligned sides, formed during LA, are clearly visible.

experimental data for an LA process of a Si(001) surface is provided, which validates the approach. The code is then applied to study the LA process in the two cases of homogeneous and inhomogeneous nucleation, varying laser fluence or pulse duration, revealing how the liquid Si nuclei evolve during laser irradiation, leading to coalescence for high nuclei densities.

RESULTS

Multiscale FEM-KMC approach

We developed a multiscale, self-consistent, fully open-source simulation tool which enables a seamless coupling of a continuum mesoscale FEM electromagnetic-thermal problem, solved using the FENICS computing platform[29], with the KMC scheme implemented in the MulSKIPS code[30–32]. Importantly, the procedure is based on a self-consistent coupling between the continuum and atomistic models, contrary to sequential coupling approaches[13], where the thermal problem is first solved over the whole pulse duration *via*, e.g., a phase-field formalism, and coupling with KMC occurs only afterwards, through mapping of the space- and time-dependent temperature into the KMC.

The general procedure is illustrated in Fig. 2 for the case of an LA process for a flat Si(001) surface. It starts by generating the FEM mesh from a user-provided computer-aided design (CAD) geometry, containing information about the regions to be atomistically modeled by KMC. For instance, in the Si(001) case considered in Fig. 2, a 19.8 μm thick Si film is modeled using a $10.8\ nm \times 10.8\ nm \times 20\ \mu m$ box periodic along the planar x, y directions. The remaining 200 nm in the FEM mesh are filled with air. The KMC region is chosen such to include only the top 30 nm of Si surface and the first 4 nm of air. Such choice of dimensions is deemed reasonable given the irradiation conditions considered in the simulations, namely 308 nm wavelength laser pulses with 160 or 20 ns duration, using fluences of 1.6–2.1 $J\ cm^{-2}$ in the former case and 1.1–1.2 $J\ cm^{-2}$ in the latter.

The external heat source and the temperature field in the FEM model are then computed at every user-defined time step Δt_{FEM} by self-consistently solving the coupled PDEs governing electromagnetic and thermal fields induced by the laser, until the melting temperature T_M is locally reached in the Si surface[13]. Thereafter an iterative procedure begins which, for the entire pulse duration and with a predefined time step $\Delta t < \Delta t_{FEM}$, couples FEM and KMC solvers in the following way:

1. The temperature field in the FEM mesh is interpolated into the (much denser) KMC super-lattice;
2. The nonhomogeneous temperature map found in step (1) is used to compute the solidification/melting probabilities of each site in the KMC super-lattice, which are then used to simulate the kinetic evolution of the solid–liquid front over Δt;
3. The atoms that undergo a phase-change during the KMC simulation are communicated to the FEM model, which again self-consistently solves the coupled Maxwell-Fourier problem while accounting for this variation;
4. The procedure restarts from step (1) and goes on for the whole pulse duration, until all atoms in the structure have resolidified.

Importantly, compared to other phase-field and enthalpy formalisms for nucleation and melting, here the main difference lies in the fact that the absorbed (released) latent heat at every time interval Δt can now be easily computed exactly by directly integrating over Δt the volume melt (resolidified) during the KMC simulations.

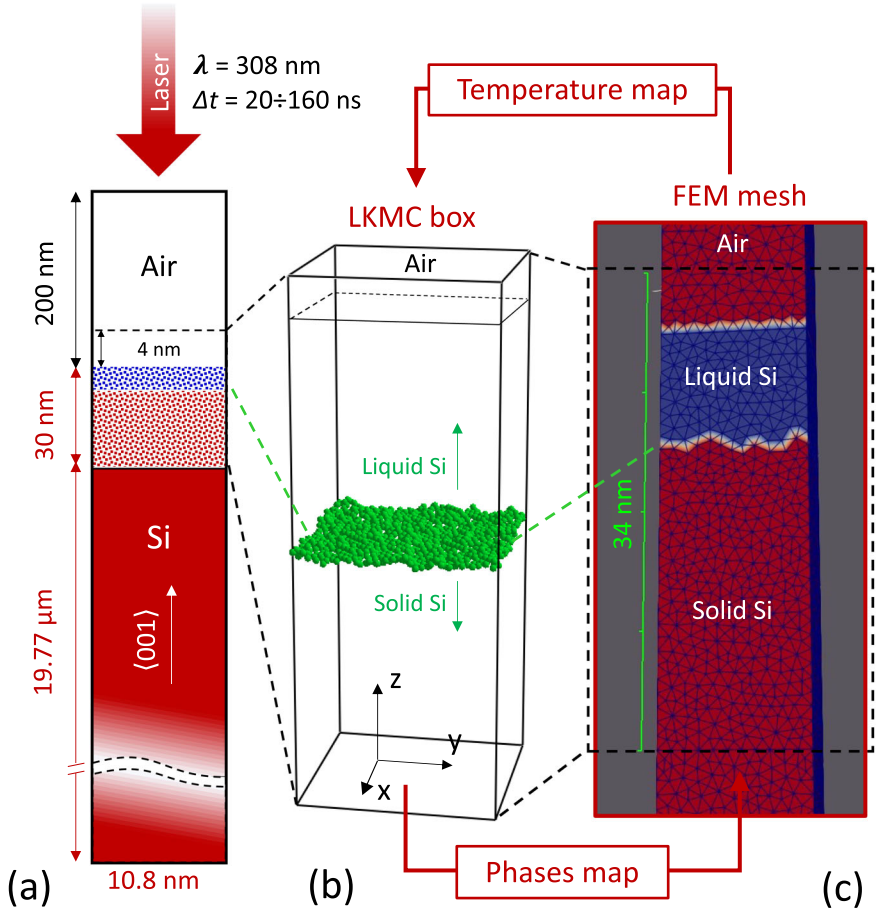


Fig. 2 Schematics of a multiscale FEM-KMC ultrafast melting simulation for a Si(001) surface. a Sketch of an input CAD geometry, with the KMC subregion indicated by the dotted area, which is blue for liquid and red for solid Si. **b** KMC system at a generic time during melting, with the solid undercoordinated Si atoms indicated in green. **c** Region of the FEM mesh corresponding to the KMC one, with liquid Si in blue and solid/air in red.

It should be noted that, at the first KMC call, an assumption should be made as far as concerns the nucleation of liquid Si. In the simplest case, the initial KMC state can be modeled to be a homogeneous thin layer of Si. In this case, we find that a minimum thickness of around 2–2.5 nm is needed to trigger a stable melting phenomenon in the MulSKIPS KMC framework. Alternatively one may consider an inhomogeneous initial nucleus, such as a small hemispherical nucleus, which represents a more realistic initial state in situations where the irradiated surface and/or the laser cross-section are not perfectly homogeneous. Simulations of both nucleation cases are reported in "Results: FEM-KMC simulations: homogeneous nucleation case" and "Results: FEM-KMC simulations: inhomogeneous nucleation case", respectively. We also note that the laser pulses considered in this work have a duration in the order of tens/hundreds of nanoseconds (much larger than the electron thermal relaxation time), so it is assumed that the energy has already been transferred from the laser to the lattice. In case of femto/picosecond laser pulses this is not true and one needs to account for electron–phonon coupling and effect of electron excitations on interatomic forces[25].

To sum up, the parameters needed for a FEM-KMC simulation can be divided into three sets. Those related to the FEM model, i.e., the physical (structural, thermal, and optical) properties of the considered material in its solid and liquid state, which we have extracted from literature[17,33,34]. Those related to the KMC model, entering the melting/solidification event frequencies, which need to be carefully calibrated until the interface velocity expected from literature is reproduced. Finally, there are a few numerical parameters involved in the communication between FEM and KMC, such as the FEM-KMC cycle time interval Δt or the mesh resolution in the region to be matched with KMC, which need to be optimized to converge the main quantities of interest, e.g., the melt-depth variation over time.

Below we summarize a few important details regarding the FEM and KMC steps of the methodology.

FEM model

In the simulations we implement a FEM model to solve self-consistently the Maxwell equations for the electromagnetic field in the irradiated system, and the Fourier's law for heat diffusion, accounting for solid–liquid phase changes and the laser pulse as irradiation heat source[35,36]:

$$\rho c_p \frac{\delta T}{\delta t} = \nabla \cdot (\kappa \nabla T(\mathbf{r}, t)) + \frac{\delta Q}{\delta t} + S(\mathbf{r}, t; T) \quad (1)$$

Here ρ is the material density, κ the thermal conductivity, c_p the specific heat at constant pressure, $\delta Q/\delta t$ the latent heat release (absorption) associated to the solidification (melting) process and $S(\mathbf{r}, t; T)$ the external heat source which, in general, implicitly depends on the thermal field due to the temperature dependent material's optical parameters, such as the complex dielectric constant for the transverse electrical mode[37]. The latter dependency is what makes the solution of the FEM model self-consistent and, in fact, non-trivial. Indeed, while in a 1D system the laser heat source may be reasonably described within a simple absorber approximation[25], systems with 2D or 3D features with size in the

order of the laser wavelength require a full self-consistent solution of Eq. (1) and Maxwell equations, in a periodic 3D box[38], to properly determine the heat source $S(\mathbf{r}, t; T)$. Such a space- and time-dependent coupling between electromagnetic and thermal fields, fully implemented in our code, is of uttermost importance to correctly describe how the laser interacts with a nanostructured material, and especially to capture how this interaction is influenced by the ultrafast atomic-scale phase changes emerging, in turn, from the complementary KMC simulations.

Lastly, the latent heat variation due to the phase transition can be written as:

$$\frac{\delta Q}{\delta t} = L\,\frac{\delta f_s(\mathbf{r}, t)}{\delta t} \tag{2}$$

where L is the latent heat of fusion and f_s is the fraction of solid at a given point in space-time. It should be noted that in Eq. (1) κ and c_p may be temperature, space and even time dependent.

KMC model

The KMC formalism used in our multiscale method is implemented in the MulSKIPS code[30]. The solid–liquid interface evolution in MulSKIPS KMC framework is regulated by the balance between solidification and melting events, whose rates are expressed as[39,40]:

$$\nu_{ls} = \nu_{ls}(\mathbf{r}, t) = \nu_0 \cdot f(T) \cdot \exp\left(\frac{-2E_n}{k_B T_M}\right) \tag{3}$$

$$\nu_{sl} = \nu_{sl}(\mathbf{r}, t) = \nu_0 \cdot \exp\left(\frac{-n \cdot (\Phi_s - \Phi_l)}{k_B T(\mathbf{r}, t)}\right) \tag{4}$$

where ν_0 is a constant prefactor, T_M is the melting temperature ($T_M = 1688$K for Si), n is the number of bonds which an interface site forms with atoms in the solid phase, and $\Phi_s - \Phi_l$ is the difference between the bond energy of two atoms binding in the solid (Φ_s) and liquid phases (Φ_l) ($\Phi_s - \Phi_l = 0.96$ eV for Si[41]). E_n is the energy barrier needed to solidify a liquid atom in a n-coordinated KMC site, with $E_{n=2} \equiv \Phi_s - \Phi_l$ to ensure equilibrium for a flat interface at $T = T_M$. Lastly, $E_{n=1}$, $E_{n=3}$, ν_0 and the T_{FV} and W_{FV} parameters in Eq. (5):

$$f(T(\mathbf{r}, t)) = \frac{1}{2}\left[1 + \mathrm{erf}\left(\frac{T(\mathbf{r}, t) - T_{FV}}{W_{FV}}\right)\right] \tag{5}$$

are chosen to reproduce the analytical Fulcher–Vogel relationship for the interface speed as a function of T fitted *via* experimental data[18,33,42–44]. Such relationship is approximately linear close to $T = T_M$, it reaches a maximum for $T < T_M$ (in the undercooling region) and monotonically increases in absolute value for $T > T_M$. Figure 3 shows how the Fulcher–Vogel profile compares with the results of KMC simulations of a melting Si(001) surface performed at constant temperature, over a wide range of temperatures, and obtained using the following calibrated set of parameters: $E_{n=1} = 0.93$ eV, $E_{n=3} = 0.99$ eV, $\nu_0 = 1.33 \times 10^{17}$, $T_{FV} = 1080$K and $W_{FV} = 280$K. As ν_{sl} and ν_{ls} depend on site coordination, the expected variation in recrystallization velocity v along different crystal orientations (e.g., $v_{[111]} < v_{[001]}$) is naturally captured by the KMC simulations. Importantly, it should be noted that the temperature $T \equiv T(\mathbf{r}, t)$ in this formulation varies in both space and time, and it is mapped directly from the results of the FEM model obtained at every time step of the FEM-KMC simulation. As a consequence, the probabilities ν_{ls} and ν_{sl} are also time- and space-dependent during the LA simulation.

It is worth pointing out that, besides the original MulSKIPS implementation reported in ref. [31], important changes have been made here in order to enable simulations of an LA process and the coupling with the FEM solver: (1) the inclusion of non-evolving regions ("wall sites") in the KMC super-lattice; (2) the possibility of reading an external CAD structure as input geometry, containing

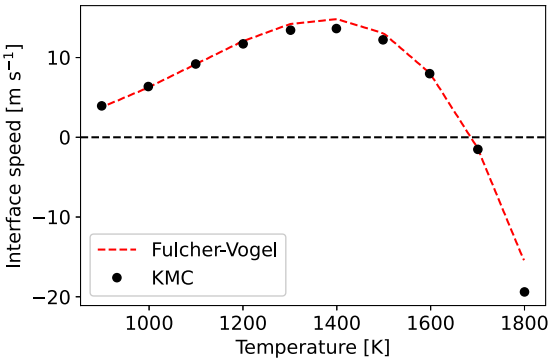


Fig. 3 Calibration of KMC model. Comparison between KMC prediction of the evolution of a Si(001) solid–liquid interface (black dots), calibrated as explained in the main text, and the Fulcher–Vogel expression for Si melting front speed (red dashed line) fitted from experimental data on crystalline Si.

the location of evolving and non-evolving regions; (3) the possibility of reading an external temperature map as input, which then is internally used to compute space- and time-dependent event probabilities for the solid–liquid KMC particles. "Wall sites" are non-evolving Monte Carlo particles whose position in the simulation box is fixed for the whole duration of the simulation, and their action is to increase by one the coordination of all nearest solid particles, which in a tetrahedral lattice would normally range from 1 to 4. As a result, for example, if an evolving Monte Carlo particle with threefold coordination ends up next to a wall-site during the simulation, it will become fully coordinated and hence will be prevented from binding to new neighbors.

FEM-KMC simulations: homogeneous nucleation case

In this section, we present simulations performed with the FEM-KMC procedure for an LA process of a Si(001) surface, assuming homogeneous nucleation. Particular focus will be given on benchmarking the method against 1D phase-field models and experiments under various LA process conditions, while describing step-by-step the multiscale procedure and highlighting some important numerical advantages of this approach with respect to continuum-based ones.

We choose a 308 nm wavelength laser pulse with 160 ns pulse duration. Figure 4a shows the $10.8 \times 10.8 \times 68.8$ nm^3 KMC cell used, with the initial solid–liquid interface (namely, all under-coordinated solid Si atoms) highlighted in green, at the onset of laser irradiation (0 ns) and at three different instants during the LA process. At 0 ns, below the interface there are 62.3 nm of solid Si, while above it there are 2.5 nm of liquid Si and 4 nm of air. We remind here that including such a thin layer of liquid Si inside the KMC box is necessary to ensure a stable onset of melting in MulSKIPS: a thinner layer would cause an almost immediate resolidification. The Si region inside the KMC box corresponds to the top 64.8 nm of a 19.735 μm thick Si film, modeled in the FEM solver using a periodic 10.8 nm × 10.8 nm × 20 μm box with 200 nm air above the initial solid surface. The resolution of the FEM mesh in correspondence of the KMC region was set to 1 nm.

The FEM simulates heating of the Si system induced by the laser pulse starting from a temperature of 300K. Once the maximum temperature T reaches $T_M = 1688$K locally in the mesh, the FEM-KMC self-consistent procedure described in "Results: multiscale FEM-KMC approach" begins. The sequence in Fig. 4a (see also Supplementary Movie 1) shows that the melting front drops ~50 nm along z after roughly 170 ns since the beginning of laser irradiation. It can be seen that the interface, as expected given the homogeneous nucleation, remains quite flat for the whole pulse

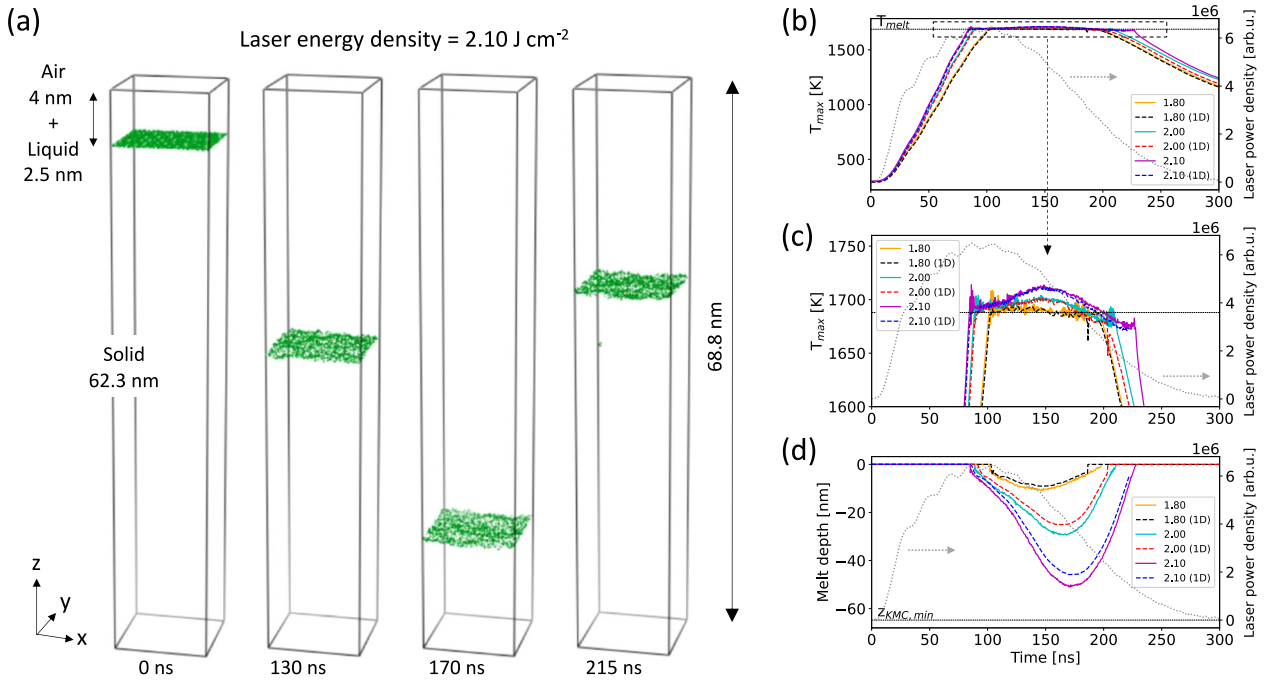


Fig. 4 FEM-KMC simulations of Si(100) laser annealing in the homogeneous nucleation case and comparison with 1D phase field. a KMC box containing all undercoordinated solid atoms (green), identifying the solid–liquid Si interface at $t = 0$, 130, 170, and 215 ns upon irradiation with a laser energy density of 2.1 J cm^{-2} (see also Supplementary Movie 1). **b** Maximum T value in the FEM mesh as a function of time (solid lines), for laser energy densities of 1.8, 2.0, and 2.1 J cm^{-2}, in comparison with the results of 1D phase-field model (dashed lines) using the same geometry and optical parameters. The power density of the laser pulse over time is also shown as black dotted line. **c** Zoom of the curves in (**b**) around T_M. **d** Variation of melt-depth over time for the same fluences (solid lines), in comparison with the results of the 1D phase-field model (dashed). The former are extracted as average z coordinate of solid Si atoms at the interface at the end of every KMC step. The maximum accessible depth for melting z_{KMC} in the KMC model is also indicated.

duration, also during the resolidification. In Fig. 4b the maximum value of temperature $T_{max}(t)$ in the whole FEM domain is plotted as a function of time, for three values of laser energy density, namely 1.8, 2.0, and 2.1 J cm^{-2}. Such maximum is located in air right above the initial solid Si surface. These profiles are plotted together with the corresponding curves obtained with standard 1D phase-field simulations performed with the same geometry and optical parameters, using the technology computer-aided design (TCAD) simulation package LASSE Innovation Application Booster (LIAB)[17]. After the initial, almost linear, heating up to $T_{max} = T_M$, one may see the expected sharp discontinuity in the slope of $T_{max}(t)$ at around 90 ns since the beginning of irradiation, which is due to the abrupt change in thermal conductivity and surface reflectivity between solid and liquid Si[33], the latter being present uniformly on top of the structure as soon as melting sets off. As can be seen in the zoom panel of Fig. 4c, a maximum T of around 2K, 10K, and 20K above T_M is reached after ~150 ns of irradiation, for 1.8, 2.0, and 2.1 J cm^{-2} fluences, respectively. Remarkably, both FEM-KMC and 1D phase-field simulations reproduce the same temperature profile during melting, despite the completely different modeling approach to phase transitions. Afterwards a linear resolidification trend begins due to the steady reduction in laser power (normalized and plotted as black dashed line in Fig. 4b–d). The latter is clearly visible in the profiles of melt-depth $\Delta z_{melt}(t)$ reported in Fig. 4d, computed as the average z coordinate of all undercoordinated solid Si atoms at the end of every KMC step. Once Si is completely solid again, in absence of irradiation the structure slowly releases the accumulated heat and thermalizes reaching room temperature after several ms from the laser pulse. We note that, besides a small overestimation of the total maximum melt depth, the FEM-KMC and 1D phase-field simulations yield almost identical results at the same fluences,

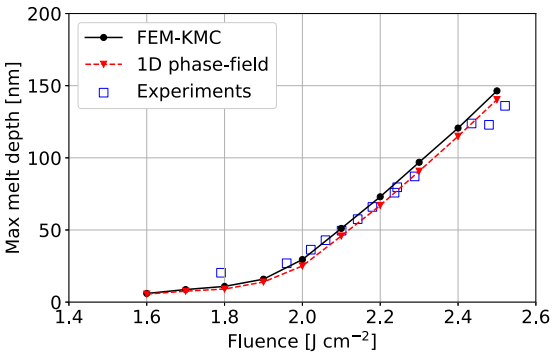


Fig. 5 Benchmark of FEM-KMC method against 1D phase-field and experiments. The maximum melt depth as a function of laser fluence is shown, simulated using the FEM-KMC and the 1D phase-field approaches, in comparison with experimental data extracted from SIMS profiles measured on a Si sample after irradiation with a 308 nm and 160 ns laser pulse.

which is a first instance of reliability of the FEM-KMC self-consistent procedure.

As a further benchmark, in Fig. 5 we plot the maximum melt depth obtained for various laser energy densities using the FEM-KMC and the 1D phase-field simulators in comparison with experimental data extracted from secondary-ion mass spectrometry (SIMS) profiles after LA for a Si sample, which was performed with a SCREEN-LT3100 pulsed XeCl excimer LA system (308 nm wavelength, 160 ns pulse duration), considering laser energy densities ranging from 1.8 to 2.6 J cm^{-2}. Both FEM-KMC and 1D phase-field simulated fluences range from 1.6 to 2.5 J cm^{-2}, at steps of 0.1 J cm^{-2}. The T_{max} and melt-depth profiles for

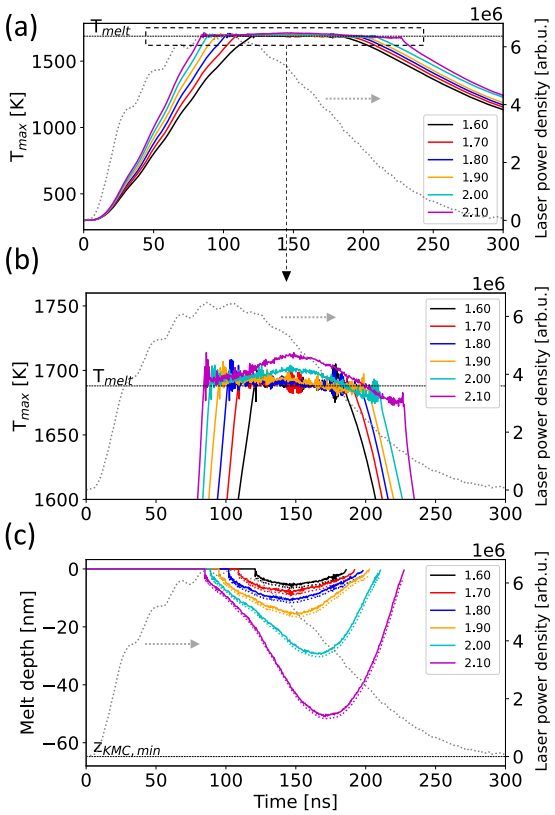


Fig. 6 FEM-KMC results for various fluences and benchmark for latent heat computation. a Maximum T value in the FEM mesh as a function of time (solid lines), for several values of laser energy density, ranging from 1.6 to 2.1 J cm^{-2}. The laser density of the laser pulse over time is also shown as black dotted line. **b** Zoom of the curves in (**a**) around T_M. **c** Variation of melt-depth over time for the same fluences, extracted as average z coordinate of solid Si atoms at the interface at the end of every KMC step (solid lines), in comparison with the melt depths estimated by means of the exchanged latent heat (dashed lines) as described in Eq. (7). The maximum accessible depth for melting in the KMC box, z_{KMC}, is also indicated as a black dashed line.

1.6–2.1 J cm^{-2} are reported in Fig. 6. The KMC cell shown in Fig. 4a, with a 68.8 nm size along z, was used for the simulations with 1.6–2.1 J cm^{-2}. This was enlarged up to 108.8 nm to enable 2.2–2.3 J cm^{-2} and to 160.2 nm to enable 2.4–2.5 J cm^{-2}, while keeping the cell xy-area constant. We find that the results of the FEM-KMC simulations are in reasonably good agreement with experiments over the whole regime of fluences. The slight deviations of FEM-KMC and 1D phase-field results from experiments may be attributed to the likely larger uncertainty in melt-depth determination close to the melting threshold and/or to the occurrence of non-ideality in the measured samples.

From a numerical point of view, an important advantage of the code relates to the computation of the heat exchanged during melting throughout the self-consistent FEM-KMC cycle. As already mentioned in "Results: multiscale FEM-KMC approach", here the main difference with respect to other LA models is that the latent heat $Q(t)$ exchanged at every time step can be computed exactly by tracking the phase-changing volume $\Delta\Omega(t)$ at every KMC step, which is now directly accessible with atomic resolution. $Q(t)$ is simply defined as

$$Q(t) = L_{Si,c} \cdot \Delta\Omega(t) \tag{6}$$

with $L_{Si,c} = 1.797 \times 10^6$ J m^{-3} being the specific latent heat of fusion per unit volume for crystalline Si. A proof of the consistency and accuracy of our simulations in this respect can be inferred

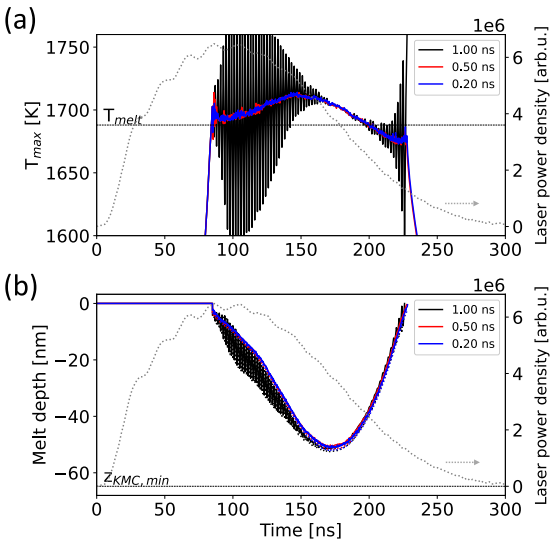


Fig. 7 Sensitivity of LA simulations to FEM-KMC cycle time interval. a Maximum T value in the FEM mesh plotted as a function of time in a range of T close to T_M, for three different values of Δt, namely 0.2 (blue), 0.5 (red), and 1 ns (black), using a fluence of 2.1 J cm^{-2}. The power density of the laser pulse over time is also shown as black dotted line. **b** Profile of melt-depth over time for the same Δt values.

from Fig. 6c, where the total melt-depth $\Delta z_{melt}(t)$, directly extracted from the output atomic coordinates of the KMC structures at $t = 0, \Delta t, 2\Delta t, \ldots$, is compared to the same quantity derived indirectly *via* Eq. (6) for $Q(t)$, using the following expression:

$$\Delta z_{melt}(t) = \frac{Q(t)}{L_{Si,c} \cdot A_{KMC}} - \Delta z_{nucleus}, \tag{7}$$

with A_{KMC} the xy area of the periodic KMC box and $\Delta z_{nucleus}$ the thickness of the uniform Si layer used as initial nucleus. The negligible differences between the two curves at all considered fluences are not only a confirmation that the computation of latent heat from the atomistic framework is correct, but also that the interpolation of the FEM mesh into the much denser KMC super-lattice is sufficiently reliable.

Compared to continuum models, an important computational advantage of FEM-KMC simulations lies in its time resolution. From the previous discussion it emerges that the choice of time interval Δt elapsing between two consecutive FEM-KMC steps during the LA self-consistent simulation is crucial for the correct computation of the latent heat. This value should be small enough to ensure a smooth variation of melting/solidifying volumes over time. However, the smaller Δt, the more time consuming is the simulation, therefore a compromise must be found. We fixed a fluence of 2.1 J cm^{-2} and plotted the maximum value of temperature in the FEM mesh as a function of time in Fig. 7a, showing the average melt-depth over time in Fig. 7b. Both quantities are plotted for three different values of Δt, namely 0.2, 0.5 and 1 ns. It can be seen that, despite all choices lead to similar average trends, using $\Delta t = 1$ ns (which is also the time interval set in the FEM simulator prior to melting) yields significantly noisy temperature and melt-depth profiles, while $\Delta t = 0.5$ ns can be identified as an optimal time interval. Interestingly, such value is larger than the value of 0.1 ns needed, e.g., to carry out the 1D phase-field LA simulations considered in Fig. 4d, which represents a clear computational advantage.

Lastly, as a reference, the relevant run-times and memory requirements for the FEM-KMC simulations of Fig. 5 are reported in Table 1. From these one can estimate what is the computational

Table 1. Summary of time and memory resources for the FEM-KMC simulations reported in Fig. 5.

L_z^{KMC} [nm]	N_{cells}	N_{DOFs}	RAM_{max} [GB]	t_{geo} [s]	$t^{\Delta t}_{FEM\to KMC}$ [s]	$t^{\Delta t}_{KMC}$ [s]	$t^{\Delta t}_{KMC\to FEM}$ [s]
68.8	586,196	152,969	6.6	587.9	5.4	101.8	21.0
108.8	604,699	156,941	7.0	980.1	5.5	145.1	23.9
160.2	629,905	162,635	7.5	1356.2	6.4	214.3	36.2

L_z^{KMC} is the KMC box size along z; N_{cells} and N_{DOFs} the number of cells and degrees of freedom (DOFs) in the input FEM mesh, respectively; RAM_{max} the maximum RAM per core needed for a simulation; t_{geo} the time spent to convert the mesh into a KMC box; $t^{\Delta t}_{FEM\to KMC}$ the time spent to map the thermal field from FEM to KMC at each FEM-KMC cycle time interval Δt, averaged over all simulations using the same KMC box; $t^{\Delta t}_{KMC}$ the average KMC runtime every Δt; $t^{\Delta t}_{KMC\to FEM}$ the average time to map the KMC atomic-scale phases back to the FEM every Δt. The total runtime for the FEM-KMC simulation is approximately given by: $\Delta t_{TOT} \equiv t_{geo} + \left[t^{\Delta t}_{FEM\to KMC} + t^{\Delta t}_{KMC} + t^{\Delta t}_{KMC\to FEM}\right] \cdot t_M/\Delta t + t_{FEM}$, with t_M being the time elapsed while melting ($T > T_M$) and t_{FEM} the sum of heating and cooling times, elapsed while $T < T_M$. All memory and time information are reported per CPU core. Simulations were run on an AMD EPYC 7742 64-Core processor.

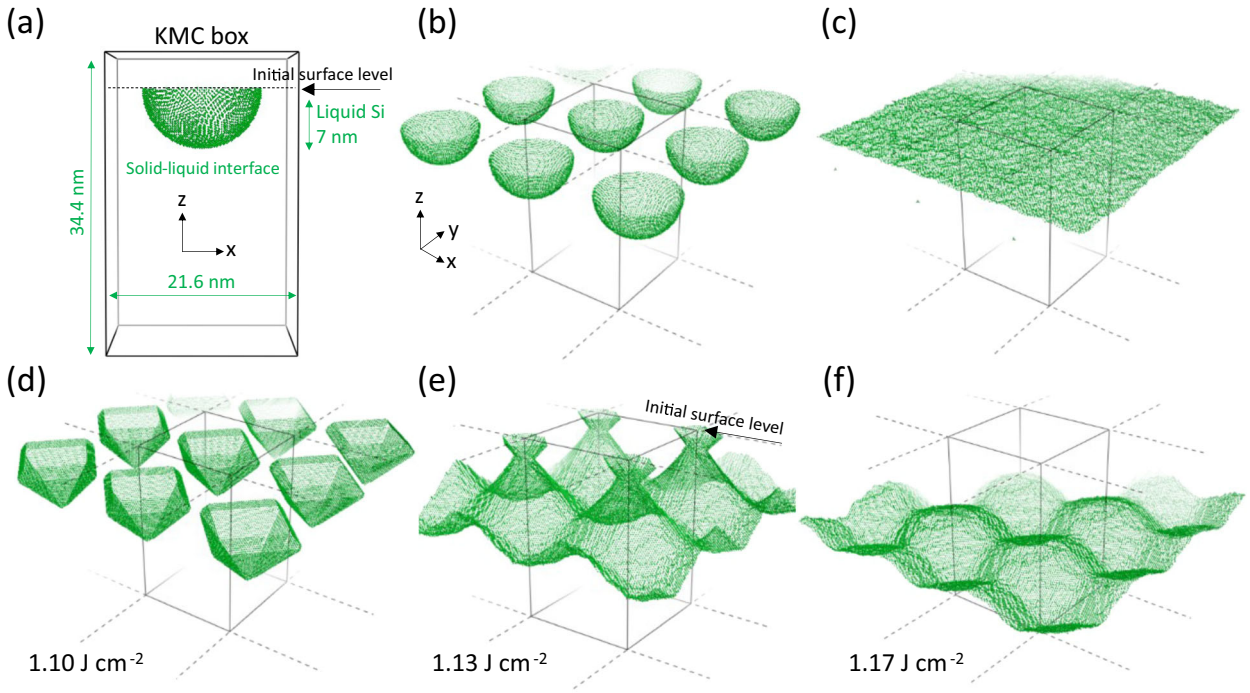


Fig. 8 FEM-KMC simulations of Si(100) laser annealing in the inhomogeneous nucleation case. a KMC periodic box used for the LA simulations with inhomogeneous nucleation, showing the solid–liquid interface in green, embedding liquid Si. The black arrow indicates the initial surface level. **b** KMC box periodically extended along x and y, highlighting the regular distribution of the initial nuclei. For convenience, here and in the following panels the top side of the box has been moved to the initial surface level. **c** Initial solid–liquid interface in the KMC box in case of homogeneous nucleation. **d** Melting front after 41 ns of irradiation at fluence 1.10 J cm^{-2}, corresponding to the time of maximum melt volume during the FEM-KMC simulation. **e** Melting front after 37 ns of irradiation at fluence 1.13 J cm^{-2} (**f**) Melting front after 32 ns of irradiation at fluence 1.17 J cm^{-2}. See also Supplementary Movies 2–4.

impact of integrating locally the KMC atomistic solver in an ultrafast melting simulation.

FEM-KMC simulations: inhomogeneous nucleation case

So far, we have always considered LA processes where nucleation of the liquid molten phase sets off homogeneously over the Si surface. In this section, we instead present the results we obtained by assuming a hemispherical shape for the initial nucleus in liquid phase placed at the interface between the Si(001) surface and air., as shown in Fig. 8a. It is worth to note that the nucleus is modeled within a box which is periodic along x and y directions, therefore the physical model which is actually simulated in this way is an infinite regular 2D array of identical nuclei, as illustrated in Fig. 8b. This is an important aspect to keep in mind when analyzing the simulations results, as there will always be interactions between periodic images of the nuclei, which can be tailored by controlling the ratio between the lateral box size and the nucleus radius.

From the considerations made in the previous section, it is understood that in case of a homogeneous nucleation the morphology of the solid–liquid melting front during the LA-induced evolution does not undergo significant structural changes, always remaining nearly flat (see Figs. 4a, 8c), with a trivial dependency on laser fluence, whose effect is solely to vary the maximum reached melt depth. On the contrary, when an initial nanometric liquid Si nucleus evolves under laser irradiation, the crystal structural symmetries might emerge and lead to a non-trivial interplay between the absorbed heat and the highly crystal-orientation-dependent energetics of the material, sometimes leading to different evolution behaviors for different laser energy densities and durations.

To investigate this we performed LA simulations using a 308 nm wavelength laser pulse with 20 ns duration. Compared to the

160 ns pulse considered in the previous sections, such short pulse provides more various and interesting scenarios in this case due to its reduced thermal budget. A periodic $21.6 \times 21.6 \times 34.4\ nm^3$ cell is used for the KMC model, with a 7 nm-radius liquid nucleus considered at the onset of melting, and 4 nm of air always present on top of the box. Given the periodic boundary conditions this is equivalent to modeling a nuclei density of roughly 2.2×10^{11} cm^{-2}. Such KMC box corresponds to the top 30.4 nm of a 19.77 µm thick Si film, modeled with a FEM mesh with 200 nm air above the solid surface. The resolution of the mesh in correspondence of the KMC region was increased to 1.5 nm to reduce the computational cost, with negligible consequences on the simulation results. Laser fluences were varied around 1.1–1.2 J cm^{-2}. The radius of 7 nm for the initial nucleus was found to be the minimal critical radius needed to observe a stable onset of melting under the considered irradiation conditions. In particular for fluences lower than 1.10 J cm^{-2} we find that, after over 26 ns of irradiation heating up to T_M, the nuclei end up re-solidifying completely in just a couple of ns. Instead, for fluences of 1.10 J cm^{-2} and above, three non-trivial evolution scenarios can be identified. Figure 8d–f shows snapshots of the results of each scenario depicting the solid–liquid interface shape at the maximum of melt volume (see also Supplementary Movies 2–4). For exactly 1.10 J cm^{-2} (see Fig. 8d) the nuclei manage to absorb enough energy from the laser to stabilize the liquid-solid interface shape. After 41 ns of irradiation, the solid Si in contact with the liquid nuclei has undergone a structural reconstruction leading to the emergence of its lowest energy {111} facets, and hence to a regular distribution of half-octahedron-shaped nuclei. We point out that such faceting along ⟨111⟩ directions was confirmed by experimental in situ observations[45] and that, from a computational point of view, it is not possible to retrieve such a faceting effect using a fully continuum approach. In fact, only thanks to the atomic resolution of the KMC solver it was possible to retrieve the flat atomic-scale morphology typical of {111} interfaces[45,46], as well as the slight atomic roughness characterizing interfaces evolving in the [001] direction (see Fig. 4). In the next 3 ns, as a result of the laser power drop, these end up rapidly solidifying. For the slightly larger fluence of 1.13 J cm^{-2} a second scenario emerges (see Fig. 8e): the nuclei not only manage to stabilize their octahedron shape, but the absorbed heat is enough to melt the Si further, until the liquid volumes touch the lateral boundaries at around 32 ns of irradiation, hence beginning to coalesce due to periodicity. As shown in Fig. 8e, this still does not lead to a uniformly thick liquid layer on top of the Si structure: even at the time of maximum melt volume, i.e., at around 37 ns of irradiation, the interface preserves the high-symmetry {111} facets and the partial coalescence leaves small octahedra of solid Si at the surface, centered around the corners of the periodic KMC box. Once undercooling begins the structure starts solidifying and ends up totally flat after roughly 43 ns of irradiation. By increasing the fluence to 1.17 J cm^{-2} and beyond a third scenario is observed (see Fig. 8f), where the stronger laser induces further melting until full coalescence is reached after no more than 32 ns of irradiation. Beyond this value of fluence, and also when longer laser pulses are used, full coalescence is always reached.

The square profile and edge-orientation along the ⟨110⟩ directions are in agreement with the images obtained *via* scanning electron microscopy (SEM) and atomic force microscopy (AFM) reported in Fig. 1a–c, regarding LA processes on bulk Si (001) at the same laser wavelength as the simulations and fluences around the onset of the surface melt regime[3]. Our simulations allowed to reveal that the ⟨110⟩-sided squared features observed experimentally are markers of an evolution in an inverse pyramidal shape of {111}-faceted octahedral molten Si nuclei existing at the early stages of melting. Furthermore, it has been found experimentally that the nuclei coalesce and cover the whole surface when increasing the laser fluence[3,11], which is also captured by our simulations (see, e.g., Fig. 8f), despite the unlikely regularity of nuclei distribution therein. We would like to remark here that such findings are a direct consequence of the atomic-scale resolution of the FEM-KMC LA simulations, and therefore could not be achieved using a fully continuum approach.

DISCUSSION

We have presented a theoretical implementation of a hybrid methodology for the full simulation of LA based on KMC simulations dealing with atomic-scale kinetics coupled with FEM solutions of the electromagnetic heat problem. The goal of this methodology is to allow for the atom-by-atom description of the melting process induced by laser, which, to the best of our knowledge, was missing in the scientific literature.

The multiscale computational procedure and the details of the FEM and KMC models have been presented. Benchmarks against continuum 1D phase-field models and experimental data have been shown, which validate the approach. The tool was applied to study LA of a Si(001) surface under various laser fluences and pulse shapes, in the two cases of homogeneous and inhomogeneous nucleation. The latter in particular marked the importance of studying melting and LA at the atomistic level, as it revealed how originally hemispherical liquid Si nuclei reshape into octahedra during the early stages of the irradiation, and how these can then evolve into localized objects with ⟨110⟩-oriented sides or coalesce and merge into a roughly flat blanket, depending on the laser fluence. The reported results suggest that, compared to fully continuum models, this is a more correct formalism to investigate the shape change effects due to the laser (melting) process.

Provided a proper calibration, the code is readily applicable to study pristine Si, Ge, and other group IV materials, however further developments at the KMC level, e.g., a redefinition of the superlattice, can extend the applicability of this framework to other crystals, and also doped or compound semiconductors (e.g., SiGe) where phase changes are characterized by segregation phenomena or the thermal response is stoichiometry dependent[11]. Lastly, we note that in this work only ultrafast melting of pristine, undefected systems has been considered. However, a remarkable feature of our KMC solver is its ability to model the formation and evolution of point and extended defects in the material during the process simulation[31,32], which is of huge interest for comparing with LA experiments in defective semiconductors. FEM-KMC simulations of defected semiconductors are in principle feasible and will be object of future investigations. Overall, the proposed multiscale methodology represents an efficient, open-source and accurate asset, easily integrated with state-of-the-art continuum-based simulators, in the quest towards a full understanding of the physics behind LA semiconductor processes.

METHODS

Simulations

The multiscale simulation tool developed in this work is distributed as part of the MulSKIPS software package[30–32]. Internally, it is based on an electromagnetic-thermal solver, implemented with a finite element method (FEM) within the FENICS computing platform[29], and a KMC solver, implemented with the MulSKIPS Fortran engine, coupled to the FEM solver by means of PyMulSKIPS, a Python interface distributed with MulSKIPS. The 1D phase-field simulations are performed using the TCAD simulation package LIAB[17].

Experiments

Surface morphology was inferred from AFM and SEM. AFM surface scans were obtained with tapping mode using a Fast-Scan Bruker tool. The scan size typically ranged from 1×1 to $10 \times 10\ µm^2$. Top-view SEM images were obtained using the secondary electrons with a SEMVision G3 system from

Applied Materials. The experimental data on growth rate are extracted from SIMS profiles obtained after performing a LA process on a Si sample using a SCREEN-LT3100 pulsed XeCl excimer laser annealing system (308 nm wavelength, 160 ns pulse duration), considering laser energy densities ranging from 1.8 to 2.6 J cm^{-2}.

DATA AVAILABILITY

The raw data supporting the findings of this study are available from the corresponding authors, upon reasonable request.

CODE AVAILABILITY

The software used and developed in this work is fully open-source. The KMC-FEM LA framework is implemented in the MULSKIPS code[30]. The input CAD geometries and their mesh are built using the gmsh software[47]. The finite element model is based on the FENICS computing platform[29]. The atomic structures are represented with V_SIM[48]. The plots are produced with Matplotlib[49].

Received: 18 October 2021; Accepted: 25 January 2022;
Published online: 11 March 2022

REFERENCES

1. Bonati, L. & Parrinello, M. Silicon liquid structure and crystal nucleation from ab initio deep metadynamics. *Phys. Rev. Lett.* **121**, 265701 (2018).
2. Bonati, L., Zhang, Y.-Y. & Parrinello, M. Neural networks-based variationally enhanced sampling. *Proc. Natl Acad. Sci. U.S.A.* **116**, 17641–17647 (2019).
3. Dagault, L. *Investigation of Si1-XGex epilayers behavior upon ultraviolet nanosecond laser annealing*. Ph.D. thesis, Université Toulouse 3 Paul Sabatier (2021).
4. Fenouillet-Beranger, C. et al. A review of low temperature process modules leading up to the first (≤500°c) planar fdsoi cmos devices for 3-d sequential integration. *IEEE Trans. Electron Devices* **68**, 3142–3148 (2021).
5. Brunet, L. et al. Breakthroughs in 3d sequential technology. In *2018 IEEE Int. Elec. Dev. Meet. (IEDM)*, 7.2.1–7.2.4 (2018).
6. Kerdilès, S. et al. (invited) sequential 3d process integration: opportunities for low temperature processing. *ECS Trans.* **80**, 215–225 (2017).
7. Lorenz, J. et al. Process variability-technological challenge and design issue for nanoscale devices. *Micromachines* **10**, 6 (2019).
8. Guerfi, Y. & Larrieu, G. Vertical silicon nanowire field effect transistors with nanoscale gate-all-around. *Nanoscale Res. Lett.* **11**, 210 (2016).
9. Cristiano, F. et al. Defect evolution and dopant activation in laser annealed si and ge. *Mater. Sci. Semicond. Process.* **42**, 188–195 (2016).
10. Stiffler, S. R., Thompson, M. O. & Peercy, P. S. Supercooling and nucleation of silicon after laser melting. *Phys. Rev. Lett.* **60**, 2519–2522 (1988).
11. Dagault, L. et al. Investigation of recrystallization and stress relaxation in nanosecond laser annealed si1-xgex/si epilayers. *Appl. Surf. Sci.* **527**, 146752 (2020).
12. La Magna, A. et al. Material modifications induced by laser annealing in two-dimensional structures. *Appl. Phys. Lett.* **84**, 4738–4740 (2004).
13. Fisicaro, G., Pelaz, L., Lopez, P. & La Magna, A. Kinetic monte carlo simulations for transient thermal fields: computational methodology and application to the submicrosecond laser processes in implanted silicon. *Phys. Rev. E* **86**, 036705 (2012).
14. Sciuto, A. et al. Phononic transport and simulations of annealing processes in nanometric complex structures. *Phys. Rev. Mater.* **4**, 056007 (2020).
15. Steinbach, I. Phase-field models in materials science. *Model. Simul. Mater. Sci. Eng.* **17**, 073001 (2009).
16. Ansari, T. Q., Huang, H. & Shi, S.-Q. Phase field modeling for the morphological and microstructural evolution of metallic materials under environmental attack. *npj Comput. Mater.* **7**, 143 (2021).
17. Huet, K. et al. Pulsed laser annealing for advanced technology nodes: Modeling and calibration. *Appl. Surf. Sci.* **505**, 144470 (2020).
18. Mittiga, A., Fornarini, L. & Carluccio, R. Numerical modeling of laser induced phase transitions in silicon. *Appl. Surf. Sci.* **154-155**, 112–117 (2000).
19. Bergmann, S., Albe, K., Flegel, E., Barragan-Yani, D. A. & Wagner, B. Anisotropic solid–liquid interface kinetics in silicon: an atomistically informed phase-field model. *Model. Simul. Mater. Sci. Eng.* **25**, 065015 (2017).
20. Buta, D., Asta, M. & Hoyt, J. J. Atomistic simulation study of the structure and dynamics of a faceted crystal-melt interface. *Phys. Rev. E* **78**, 031605 (2008).
21. Pohl, J., Müller, M., Seidl, A. & Albe, K. Formation of parallel (111) twin boundaries in silicon growth from the melt explained by molecular dynamics simulations. *J. Cryst. Growth* **312**, 1411–1415 (2010).
22. Yeh, W., Shirakawa, T., Pham, A. H. & Morito, S. Twin formation in micro-chevron laser beam scanning induced one directional crystal growth in si film on SiO2. *Jpn. J. Appl. Phys.* **59**, SGGJ05 (2020).
23. Sun, Z. & Gupta, M. C. A study of laser-induced surface defects in silicon and impact on electrical properties. *J. Appl. Phys.* **124**, 223103 (2018).
24. Miller, W. & Popescu, A. Micro structures in the grain evolution during solidification of silicon: Phase field calculations. *Acta Mater.* **140**, 1–9 (2017).
25. Fisicaro, G. & La Magna, A. Modeling of laser annealing. *J. Comput. Electron.* **13**, 70–94 (2014).
26. Thompson, M. O. et al. Melting temperature and explosive crystallization of amorphous silicon during pulsed laser irradiation. *Phys. Rev. Lett.* **52**, 2360–2363 (1984).
27. Murakami, K., Eryu, O., Takita, K. & Masuda, K. Explosive crystallization starting from an amorphous-silicon surface region during long pulsed-laser irradiation. *Phys. Rev. Lett.* **59**, 2203–2206 (1987).
28. Sciuto, A. et al. Advanced simulations on laser annealing: explosive crystallization and phonon transport corrections. In *Int. Conf. Simul. Semicond. Process. Devices SISPAD*, 71–74 (2020).
29. Alnæs, M. et al. The fenics project version 1.5. *Archive of Numerical Software* **3** (2015).
30. Calogero, G., Deretzis, I., Fisicaro, G. & La Magna, A. Mulskips. https://github.com/MulSKIPS/MulSKIPS (2021).
31. La Magna, A. et al. Simulation of the growth kinetics in group iv compound semiconductors. *Phys. Status Solidi A* **216**, 1800597 (2019).
32. Fisicaro, G. et al. Genesis and evolution of extended defects: The role of evolving interface instabilities in cubic sic. *Appl. Phys. Rev.* **7**, 021402 (2020).
33. La Magna, A. et al. A phase-field approach to the simulation of the excimer laser annealing process in si. *J. Appl. Phys.* **95**, 4806–4814 (2004).
34. Okhotin, A., Pushkarskii, A. & Gorbachev, V. V. *Thermophysical Properties of Semiconductors* (Moskov: Atom Publ. House, 1972).
35. Rappaz, M. Modelling of microstructure formation in solidification processes. *Int. Mater. Rev.* **34**, 93–124 (1989).
36. La Magna, A. et al. Ultra-shallow junction by laser annealing: integration issues and modelling. *Nucl. Instrum. Methods Phys. Res. B* **253**, 1–8 (2006).
37. Jellison, G. E. & Modine, F. A. Optical functions of silicon at elevated temperatures. *J. Appl. Phys.* **76**, 3758–3761 (1994).
38. Sullivan, D. M. *Electromagnetic Simulation Using the FDTD Method* (IEEE Press, 2000).
39. Jackson, K. A., Gilmer, G. H. & Temkin, D. E. Monte carlo simulation of the rapid crystallization of bismuth-doped silicon. *Phys. Rev. Lett.* **75**, 2530–2533 (1995).
40. La Magna, A. et al. Vacancy generation in liquid phase epitaxy of si. *Phys. Rev. B* **75**, 235201 (2007).
41. Woodraska, D. L. & Jaszczak, J. A. A monte carlo simulation method for 111 surfaces of silicon and other diamond-cubic materials. *Surf. Sci.* **374**, 319–332 (1997).
42. Fulcher, G. S. Analysis of recent measurements of the viscosity of glasses. *J. Am. Ceram. Soc.* **8**, 339–355 (1925).
43. Vogel, D. Das temperaturabhaengigkeitsgesetz der viskositaet von fluessigkeiten. *Phys. Z.* **22**, 645 (1921).
44. Stiffler, S., Evans, P. & Greer, A. Interfacial transport kinetics during the solidification of silicon. *Acta Metall. Mater.* **40**, 1617–1622 (1992).
45. Yang, X. et al. Crystal growth and equilibrium crystal shapes of silicon in the melt. *Prog. Photovolt. Res. Appl.* **22**, 574–580 (2014).
46. Reitano, R., Smith, P. M. & Aziz, M. J. Solute trapping of group iii, iv, and v elements in silicon by an aperiodic stepwise growth mechanism. *J. Appl. Phys.* **76**, 1518–1529 (1994).
47. Geuzaine, C. & Remacle, J.-F. Gmsh: A 3-d finite element mesh generator with built-in pre- and post-processing facilities. *Int. J. Numer. Methods Eng.* **79**, 1309–1331 (2009).
48. CEA. V_sim. https://www.mem-lab.fr/en/Pages/L_SIM/Softwares/V_Sim.aspx (2021).
49. Hunter, J. D. Matplotlib: a 2d graphics environment. *Comput. Sci. Eng.* **9**, 90–95 (2007).

ACKNOWLEDGEMENTS

We gratefully acknowledge funding from the European Union's Horizon 2020 Research and Innovation program under grant agreement No. 871813 MUNDFAB.

AUTHOR CONTRIBUTIONS

A.L.M., G.C., G.F., and I.D. developed the kinetic Monte Carlo code and outlined the formalism behind the multiscale modeling approach. G.C. and A.L.M. implemented the multiscale model. D.R. and G.C. performed the calibration of the kinetic Monte Carlo code. G.C. performed the laser annealing multiscale simulations. A.S. performed

the 1D phase-field simulations. F.C., S.K., P.A.A., and K.H. provided the experimental data. G.C. prepared the figures and wrote the main paper text. All authors discussed the results and participated to the writing and the reviewing of the paper.

COMPETING INTERESTS

The authors declare no competing interests.

ADDITIONAL INFORMATION

Supplementary information The online version contains supplementary material available at https://doi.org/10.1038/s41524-022-00720-y.

Correspondence and requests for materials should be addressed to Gaetano Calogero or Antonino La Magna.

Reprints and permission information is available at http://www.nature.com/reprints

Publisher's note Springer Nature remains neutral with regard to jurisdictional claims in published maps and institutional affiliations.

Open Access This article is licensed under a Creative Commons Attribution 4.0 International License, which permits use, sharing, adaptation, distribution and reproduction in any medium or format, as long as you give appropriate credit to the original author(s) and the source, provide a link to the Creative Commons license, and indicate if changes were made. The images or other third party material in this article are included in the article's Creative Commons license, unless indicated otherwise in a credit line to the material. If material is not included in the article's Creative Commons license and your intended use is not permitted by statutory regulation or exceeds the permitted use, you will need to obtain permission directly from the copyright holder. To view a copy of this license, visit http://creativecommons.org/licenses/by/4.0/.

© The Author(s) 2022